

# Modeling seasonal variations of auroral particle precipitation in a global-scale magnetosphere-ionosphere simulation

M. Wiltberger,<sup>1</sup> R. S. Weigel,<sup>2</sup> W. Lotko,<sup>3</sup> and J. A. Fedder<sup>4</sup>

Received 20 February 2008; revised 8 September 2008; accepted 6 November 2008; published 14 January 2009.

[1] A variety of observations have shown strong seasonal variations in a vast array of magnetosphere-ionosphere parameters, including field-aligned currents, cross polar cap potential, and precipitating electron energy flux. In this paper we examine how these variations are modeled in the Lyon-Fedder-Mobarry (LFM) global-scale magnetohydrodynamic simulation of the coupled solar wind-magnetosphere-ionosphere system. In order to account for changes in the solar wind conditions caused by the seasonal variation of the Earth's dipole tilt we carefully select the solar wind parameters so that the effective driving conditions are the same across the March, June, and December intervals examined. The seasonal variation of the field-aligned current strengths is in good agreement with observations, with the sunlit hemisphere having more current than the dark hemisphere in the June and December intervals. However, in order to bring the modeled precipitating electron energy flux into better agreement with the observations we need to utilize a modified current-voltage relationship which includes a proxy for illumination effects. We provide a detailed description of the LFM's magnetosphere-ionosphere coupling interface including how illumination effects are incorporated into the model. This methodology for including these effects does not allow for determining if changes in conductance or ionospheric density are responsible for the changes. In addition to improving the agreement with observations the new version of the current-voltage relationship results in enhanced geomagnetic activity in the March interval examined and suppression of activity during the June interval.

**Citation:** Wiltberger, M., R. S. Weigel, W. Lotko, and J. A. Fedder (2009), Modeling seasonal variations of auroral particle precipitation in a global-scale magnetosphere-ionosphere simulation, *J. Geophys. Res.*, *114*, A01204, doi:10.1029/2008JA013108.

## 1. Introduction

[2] Activity within the magnetosphere-ionosphere system is regulated by several factors including solar wind driving and EUV illumination of the ionosphere. The amount of energy and momentum being transferred into the magnetosphere has long been known to be controlled by the strength and direction of the interplanetary magnetic field (IMF) as well as the solar wind velocity [Fairfield and Ness, 1967; Kan and Lee, 1979; Akasofu, 1981]. The field aligned current systems created by this interaction couple the magnetosphere with the ionosphere. In a simple circuit analogy [e.g., Kelley, 1989], the generator is the solar wind and the ionosphere is a load with its conductance regulating the amount of energy dissipated. More sophisticated circuit models [e.g., Horton and Doxas, 1998] include the effects

of current systems originating in the magnetotail. One important aspect of these currents is the creation of the aurora and its associated particle precipitation which modifies the ionospheric conductivity and Joule dissipation, thereby feeding back on the magnetosphere. The goal of this work is to model electrodynamical aspects of magnetosphere-ionosphere coupling on a global scale with an emphasis on its seasonal variation.

[3] Theoretical and experimental work characterizing the magnetosphere-ionosphere interaction has a long history. Knight [1973] developed a current-voltage relationship for upward flowing currents which described the parallel potential drop needed to accelerate the relatively low-density magnetospheric electrons to energies required to supply the current. This work was confirmed by the rocket observations of electron precipitation reported by Lyons *et al.* [1979]. This relationship and observation constitutes one of the pillars of modeling magnetosphere-ionosphere (MI) coupling. More recent work has shown that potential drops also occur in regions of downward currents [Temerin and Carlson, 1998; Andersson *et al.*, 2002; Paschmann *et al.*, 2003; Cattell *et al.*, 2004].

[4] The level of geomagnetic activity as measured by a variety of indices, e.g., AE, Dst, Kp, has a semiannual variation, with higher activity occurring near the equinoxes. Russell and McPherron [1973] developed an explanation

<sup>1</sup>High Altitude Observatory, National Center for Atmospheric Research, Boulder, Colorado, USA.

<sup>2</sup>Department of Computational and Data Sciences, George Mason University, Fairfax, Virginia, USA.

<sup>3</sup>Thayer School of Engineering, Dartmouth College, Hanover, New Hampshire, USA.

<sup>4</sup>Icarus Research Inc., Bethesda, Maryland, USA.

for this variation which relies upon the seasonal variation of the Earth's tilt and how it interacts with the IMF. The basic idea of the Russell-McPherron effect is that because the IMF is on average oriented along the Parker spiral direction, the tilt of the Earth's dipole interacting with this field results in a geoeffective GSM  $B_Z$  component of the magnetic field. The annual variation of this interaction results in a peak near equinox. In particular, the IMF direction must be pointed toward the Earth during the March equinox and away from the Earth during the September equinox so that the resulting GSM  $B_Z$  magnetic field is southward. Certain aspects of this explanation have been challenged many times [Mayaud, 1974; Berthelier, 1990; Cliver *et al.*, 2000; Newell *et al.*, 2002]. Weigel [2007] showed that in the auroral zone at least 50% of seasonal variation is not explained by the Russell-McPherron effect. Despite these concerns any effort to include seasonal variations in global-scale models must account for this fundamental interaction.

[5] Ionization by extreme ultraviolet (EUV) solar radiation creates a conductance profile in the ionosphere which is controlled, in part, by the solar zenith angle. This leads to a seasonal and universal time (UT) variation. Newell *et al.* [1996] used charged particle data from instruments aboard Defense Meteorological Satellite Program (DMSP) satellites to determine that EUV ionization tends to suppress discrete aurora. Using Polar UVI observations, Liou *et al.* [2001] determined that hemispheric power in electron precipitation is smaller on the nightside of the sunlit (summer) hemisphere than in the unlit (winter) hemisphere. Newell *et al.* [2002] proposed an explanation for the semiannual variation of the geomagnetic activity based upon the observation that the suppression of discrete aurora by EUV illumination would lead to more activity near the equinoxes since both hemispheres would have the auroral zone in darkness. Some of this activity may be attributed to an ionospheric feedback instability, which stimulates enhanced electron precipitation on field lines threading low-conductance regions of the ionosphere [Pokhotelov *et al.*, 2002].

[6] Satellite observations in the low-altitude magnetosphere show that the plasma density in this region exhibits a similar variation with season, MLT, and EUV intensity [Johnson *et al.*, 2001; Morooka and Mukai, 2003]. Numerous studies have examined the effects of lower density on the potential drop in regions of downward flowing electrons [Johnson *et al.*, 2003; Hull *et al.*, 2003; Morooka and Mukai, 2003; Cattell *et al.*, 2006]. Using observations from the Akebono satellite, Morooka and Mukai [2003] noted a significant seasonal variation in both the altitude and occurrence frequency of electron acceleration. However, they noted no clear seasonal variation in the magnitude of the field-aligned potential difference and concluded that the frequency of auroral acceleration is likely controlled by the seasonal changes in density at the ionospheric end of the field line where acceleration is occurring. Cattell *et al.* [2006] used FAST observations to determine that illumination results in lower characteristic energy electron beams on the dayside than those on the night side by factor of nearly two. They also noted that the reduction in the occurrence frequency of electron beams only occurs in beams with energy fluxes greater than a few  $\text{erg}/\text{cm}^2 \text{ s}$ . These results indicate a strong dependence of parallel potential drops on the ionospheric density and scale height.

[7] Global-scale magnetohydrodynamic (MHD) simulations of the solar wind-magnetosphere-ionosphere interaction have been used to simulate a variety of geomagnetic responses ranging from substorms [Lopez *et al.*, 1998; Wiltberger *et al.*, 2000] to storms [Goodrich *et al.*, 1998; Raeder *et al.*, 2001] and have been quantitatively compared against observations [Ridley *et al.*, 2002; Huang *et al.*, 2006]. A major strength of these simulations is that in addition to describing the interaction of the solar wind with the magnetosphere they also include ionospheric models which allow magnetosphere-ionosphere coupling to be examined. It is also possible to control the incoming solar wind parameters and ionospheric conductance to conduct controlled experiments and to quantify the factors that regulate the magnetosphere-ionosphere system [Wiltberger *et al.*, 2005a].

[8] In this paper we examine the seasonal changes in magnetosphere-ionosphere coupling due to ionospheric effects by investigating the results from global-scale simulations. We test an ionospheric model that includes the effects of seasonal changes on the acceleration of electrons into the ionosphere. In section 2 we describe, in detail, how magnetosphere-ionosphere coupling is modeled by the Lyon-Fedder-Mobarry (LFM) simulation. We also present modifications to this model which allow seasonal affects to be directly included. In addition, we explain how the solar wind conditions are chosen to eliminate the Russell-McPherron effect while still allowing for seasonal changes in the solar illumination. Section 3 compares a series of simulation intervals with and without the seasonal modifications to the MI coupling interface. A brief summary is given in the final section of the paper.

## 2. Simulation Information

[9] As described by Lyon *et al.* [2004], the LFM model uses several techniques to model the SW-M-I system. At its core it uses ideal MHD to simulate the interaction between the solar wind and magnetosphere. It uses advanced numerical techniques, e.g., the partial donor method [Hain, 1987], a nonuniform finite volume grid, and the Boris correction [Boris, 1970] to provide a robust, accurate and efficient simulation of the magnetosphere. In addition, it includes a 2D electrostatic model of the ionosphere to simulate MI coupling [Fedder *et al.*, 1995]. The basis of this model is Ohm's Law and the current continuity equation which are integrated over the height of the ionosphere. These equations, combined with the electrostatic condition  $\vec{E} = -\nabla_{\perp}\Phi$ , imply

$$\nabla_{\perp} \cdot (\bar{\Sigma} \cdot \nabla_{\perp} \Phi) = J_{\parallel} / \sin(I) \quad (1)$$

$J_{\parallel}$  is the field-aligned current (FAC) at the ionospheric height flowing between the magnetosphere and ionosphere,  $\Phi$  is electric potential, and  $I$  is the magnetic inclination angle. The final element of this model is the specification of the ionospheric conductance,  $\bar{\Sigma}$ , which contains components from EUV ionization and particle precipitation. After solving the Poisson equation for the electric potential, it is mapped along dipole field lines to the MHD simulation boundary located at a geocentric radial distance of  $2 R_E$ . The electric field computed from this potential serves as a boundary condition for the magnetospheric MHD solution.

[10] While the LFM ionospheric model has been described previously [Fedder *et al.*, 1995; Slinker *et al.*, 1999; Wiltberger *et al.*, 2003], we provide a detailed discussion here to facilitate interpretations of the simulation results described in the next section. The LFM uses an EUV conductance model similar to the one used in the AMIE model [Richmond, 1992]. This model has a spatially varying conductance profile that is parameterized by the solar EUV flux as indicated by the 10.7 cm flux and the instantaneous solar zenith angle. The EUV conductance is locally augmented by the effects of electron precipitation with properties derived from LFM's dynamically calculated MHD variables at the low-altitude simulation boundary.

[11] According to the basic kinetic theory developed by Knight [1973] and extended by Fridman and Lemaire [1980], the number flux of electrons in the loss cone at the ionospheric altitude precipitating from a source region in the magnetosphere is given by

$$F = N_e \left( \frac{k_B T_e}{2\pi m_e} \right)^{1/2} \frac{B_I}{B_M} \cdot \left\{ 1 - \left( 1 - \frac{B_M}{B_I} \right) \exp \left[ \frac{-eV}{k_B T_e \left( \frac{B_I}{B_M} - 1 \right)} \right] \right\}, \quad (2)$$

where  $e$  and  $m_e$  are the electron charge and mass,  $k_B$  is Boltzman's constant,  $T_e$  and  $N_e$  are the electron temperature and density in the magnetospheric source region,  $B_M$  and  $B_I$  are the magnetic field strengths at the source region and in the ionosphere, and  $V$  is the parallel potential drop along the magnetic field line connecting these regions. In the case when the potential drop is zero the flux is simply

$$F = N_e \left( \frac{k_B T_e}{2\pi m_e} \right)^{1/2}. \quad (3)$$

[12] In order to evaluate the number flux of precipitating electrons predicted by equation (2) we use MHD variables from the LFM simulation to constrain the parameters appearing in equation (2). The first step is to calculate the electron thermal energy,  $\mathcal{E}_M$ , in the magnetospheric source region at the inner boundary, approximately 1  $R_E$  above the ionosphere. For this purpose, we set

$$\mathcal{E}_M = k_B T_e = \alpha c_s^2, \quad (4)$$

where the parameter  $\alpha$  relates the electron temperature to the single fluid sound speed,  $c_s$ , readily available from the MHD computation. Using the  $V = 0$  limit given by equation (3), we set the initial number flux  $F_o$  to be

$$F_o = \beta \rho \mathcal{E}_M^{1/2}, \quad (5)$$

where  $\rho$  is the plasma mass density obtained from the MHD computation at the inner boundary. The parameter  $\beta$  effectively specifies the degree of loss cone filling in the electron source region.

[13] To specify the potential drop  $V$  in equation (2), we assume  $V$  is linearly proportional to the field-aligned current

$J_{\parallel}$  flowing at the simulation's inner boundary. More specifically, we set

$$\mathcal{E}_{\parallel} = eV = \frac{R \mathcal{E}_M^{1/2}}{\rho} J_{\parallel}, \quad (6)$$

where the parameter  $R$  is determined by an anomalous resistivity. The equations and assumptions leading to the formulation of equation (6) are discussed in more detail in Appendix A. The acceleration region embodied in equation (6) is assumed to be a thin anomalous resistive layer located near the MHD simulation boundary.

[14] As already noted, observations show a strong dependence of electron precipitation on solar illumination and these effects are not directly included in the parallel energy given in equation (6). While the exact mechanism is not completely understood we know that in regions of EUV illumination the energy and energy flux of precipitating electrons is reduced, so it is desirable to model these effects in the simulation. From the current-voltage relation (6), the energy gained by precipitating electrons is inversely proportional to the MHD density at the simulation boundary. The effect of EUV illumination on the precipitation flux may be modeled by modifying this density dependence. To this end, we define

$$\rho_{\max} = \max(\eta \Sigma_P, \rho) \quad (7)$$

where  $\Sigma_P$  is the EUV driven component of the ionospheric Pedersen conductance, used as a proxy for the amount of solar illumination, since it is readily available within the simulation. The parameter  $\eta$  is an adjustable conversion factor that serves to limit the energization of precipitating electrons.

[15] With  $\rho$  replaced by  $\rho_{\max}$  in equation (6), the EUV limited energization of precipitating electrons is determined by

$$\mathcal{E}'_{\parallel} = eV = \frac{R \mathcal{E}_M^{1/2}}{\rho_{\max}} J_{\parallel}. \quad (8)$$

We see that for low solar illumination ( $\eta \Sigma_P < \rho$ ) the current-voltage relation is unchanged, whereas for high illumination ( $\eta \Sigma_P > \rho$ ), the potential drop is limited. It is important to note that while the parameter  $\eta$  specifies the strength of this interaction, it does not directly address the physical mechanism of the regulation. It simply assumes that when the illumination is high, the acceleration of precipitating electrons by a field aligned potential drop is moderated. In the next section, we compare simulation results using equation (6) with those obtained using equation (8) for the energization of precipitating electrons.

[16] Recalling that the ionospheric potential serves as the inner boundary condition for the MHD magnetospheric simulation and that this potential is determined by the solution of equation (1) we need to specify the conductance tensor

$$\bar{\Sigma} = (\bar{I} - \hat{b}\hat{b})\Sigma_P + \bar{I} \times \hat{b}\Sigma_H, \quad (9)$$



**Table 1.** Solar Wind Conditions at Dipole Tilt Angles Which Have Been Selected So That the Same GSM Fields Are Imposed on the Magnetopause Regardless of the Tilt Angle<sup>a</sup>

	$V_X$	$V_Y$	$V_Z$	$B_X$	$B_Y$	$B_Z$
$-3.41^\circ$ (20 Mar, 1030 UT)	-399	0	24	1.82	-2.00	-3.11
$34.4^\circ$ (20 Jun, 1700 UT)	-330	0	-226	3.34	-2.00	-1.35
$-34.4^\circ$ (21 Dec, 0430 UT)	-330	0	226	-0.0447	-2.00	-3.61
GSM values	-400	0	0	2.00	-2.00	-3.00

<sup>a</sup>Velocities are in km/s, and magnetic fields are in nT.

where is  $\bar{I}$  the unit tensor,  $\hat{b}$  is the local unit vector in the direction of the magnetic field, and  $\Sigma_P$  and  $\Sigma_H$  are the Pedersen and Hall conductances. For this purpose, we use the empirical relationships developed by *Robinson et al.* [1987]

$$\Sigma_P = \frac{40\bar{\mathcal{E}}}{16 + \bar{\mathcal{E}}^2} \Phi_E^{1/2}, \quad (10)$$

$$\Sigma_H = 0.45\bar{\mathcal{E}}^{0.85}\Sigma_P, \quad (11)$$

to determine the electron precipitation contributions to the Pedersen and Hall conductance needed to calculate the potential. In order to use these relationships we calculate the average energy,  $\bar{\mathcal{E}}$ , of the precipitating electrons as

$$\bar{\mathcal{E}} = \mathcal{E}_M + \mathcal{E}_\parallel \quad (12)$$

or

$$\bar{\mathcal{E}} = \mathcal{E}_M + \mathcal{E}'_\parallel \quad (13)$$

and the energy flux,  $\Phi_E$ , as

$$\Phi_E = \bar{\mathcal{E}}F \quad (14)$$

where  $F$  is computed from equation (2) using either equation (6) or (8) respectively, when equation (12) or (13) is used for  $\bar{\mathcal{E}}$ . As a practical matter, in the LFM model the density, sound speed, and FACs at the MHD boundary are mapped along dipole field lines to the ionospheric grid and are then used as needed within the LFM precipitation model. The adjustable parameters,  $\alpha$ ,  $\beta$ ,  $R$ , and  $\eta$ , have been chosen in previous studies to optimize the agreement between simulation results and by observations [e.g., *Fedder et al.*, 1995; *Slinker et al.*, 1999]. These same values for the parameters are used here:  $\alpha = 1.03$ ,  $\beta = 0.436$ ,  $R = 8.37 \cdot 10^{-2}$ , and  $\eta = 1.65 \cdot 10^{-24}$ .

[17] Another key feature of the LFM model is its ability to handle temporally varying upstream boundary conditions. The plasma and magnetic field parameters along the upstream and outer edges of the computational volume are based on solar wind conditions, which can be obtained from spacecraft observations or specified as idealized configurations. The solenoidal nature of the magnetic field introduces a complication in the implementation of these boundary conditions. The front edge of the computational boundary is a two dimensional surface so the magnetic field can only have variations in the components contained in that plane. If we assume the  $X$  direction is normal to the front boundary

of the computational domain it is impossible to compute  $\partial B_X / \partial x$ , so variations are only possible in the  $B_Y$  and  $B_Z$  components of the magnetic field. This constraint can be relaxed slightly by determining a  $B_X$  which is a function of  $B_Y$  and  $B_Z$  and is the best fit to the original  $B_X$  [*Lyon et al.*, 2004]. This procedure has the net result of creating a new plane along which the normal component of the magnetic field has no variations, thus keeping the input magnetic field divergence free. This planar front is then propagated into the computational domain. In order to isolate the effect of solar-induced variations in conductance from the effect of changes in the average solar wind conditions on the magnetospheric response, we need to specify a set of solar wind parameters which result in the same GSM values for the solar wind velocity and magnetic field regardless of season. Since the simulation uses SM coordinates and MI coupling is best ordered in the GSM coordinates, we must find a set of SM values at each time step that results in constant GSM values. Consistent with the work of *Russell and McPherron* [1973] we include an IMF  $B_X$  and  $B_Y$  component in the magnetic field. In order to simplify the analysis and avoid complications arising from the transformation from SM to GSM with a time varying  $B_X$  component, we selected three discrete dipole tilt angles,  $-3.41^\circ$  (March equinox),  $34.4^\circ$  (June solstice) and  $-34.4^\circ$  (December solstice), and held them fixed while the solar wind propagates through the computational domain. In Table 1 we show the values of the solar wind conditions that result in the same GSM parameters at these dipole tilts.

### 3. Results and Discussion

[18] The dipole tilt angle for each season was thus held fixed and the solar wind variables have the same GSM values regardless of the dipole tilt angle. In each case we ran the simulation through the same start up sequence before imposing the final interval of southward IMF on the magnetosphere. The input solar wind conditions begin with a 50 min interval of no IMF, followed by a 2 h interval with southward IMF, and then a 2 h interval with northward IMF. After the northward IMF interval, the IMF stays southward for the remaining 4 h in the simulation period. We define the beginning of simulation time, 0000 ST, as the arrival of the first period of southward IMF at the Earth. In order to compare the effects of the EUV illumination model on the energization of precipitating electrons, we have completed two sets of these simulations. In the first set, hereafter referred to as EUV CV Model, equation (8) was used as part of the calculation for the average energy of precipitating electrons. In the second set, hereafter referred to as Basic CV Model, equation (6) was used for this calculation.

[19] Figure 1 shows the configuration of the magnetosphere and ionosphere at the dipole tilt angles considered in this study. The magnetospheric configuration in the March

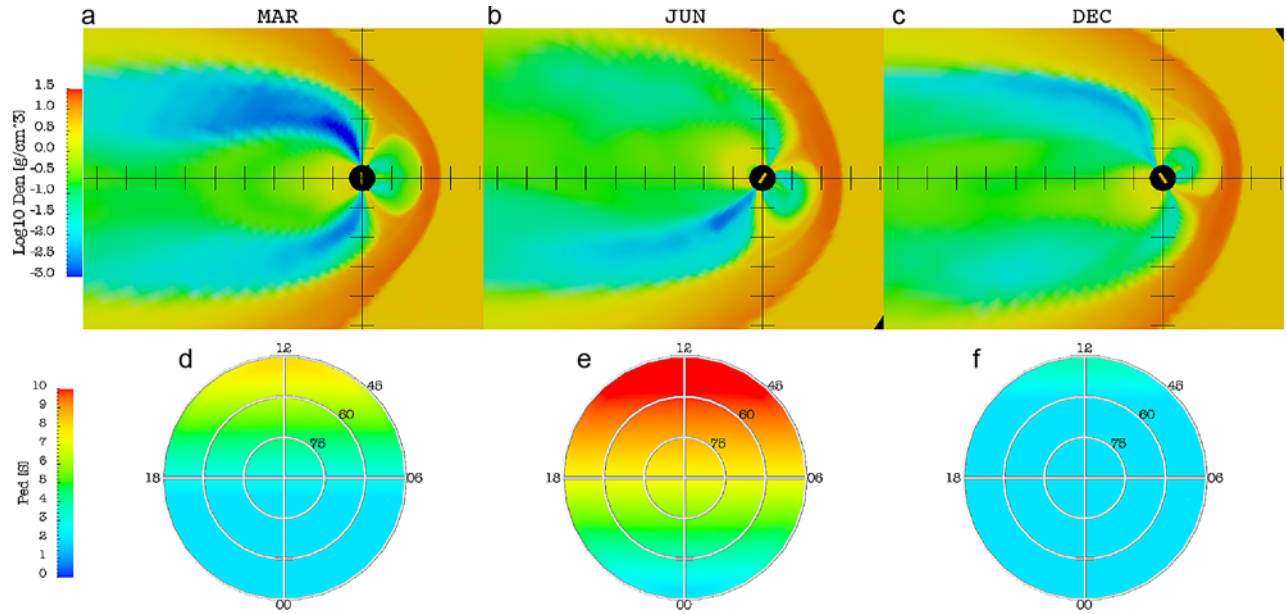


**Figure 1.** Configuration of the magnetosphere and ionosphere at the three dipole tilts examined in this work. (a–c) A cut through the XZ GSM plane of the magnetosphere colored with the log of plasma density. (d–f) The Pedersen conductance in the Northern Hemisphere ionosphere. In Figures 1a and 1d the configuration for March is shown, June solstice is shown in Figures 1b and 1e, and Figures 1c and 1f contain the December solstice.

interval is very symmetric with clearly defined cusps going into both hemispheres. The lobe connected to the Northern Hemisphere has a slightly lower density which is due to the slight dipole tilt angle present. The Pedersen conductance shows that the night side auroral oval is not illuminated by the sun and has very low conductance. The June and December solstice cases are nearly mirror images of each other in terms of the magnetospheric configuration. The hemisphere pointing into the solar wind exhibits a denser cusp while the hemisphere pointing away from the solar wind has a much lower lobe density. The June interval Northern Hemisphere ionosphere exhibits a high conductance which extends past the dawn/dusk line well into the auroral zone on the night side. On the other hand, the December interval has low conductance due to the weak solar illumination. In all of these configurations only the EUV conductance is shown. A minor point regarding all the conductance plots is that the local conductance has a floor of 2 mhos, which is imposed to keep the ionospheric solver numerically stable. This floor modifies the total transpolar potential on the order of 10% or less and dramatically improves the performance of the solver.

[20] Figure 2 shows two integrated diagnostics from the two sets of simulation results using equations (6) and (8) for the energization of precipitating electrons. The cross polar cap potential,  $\Phi_C$ , was determined by computing the difference between the maximum and minimum potential at that instant in time. The positive FAC was computed by integrating the positive FACs over the entire polar cap. Notice that in all cases the currents and  $\Phi_C$  increase after the IMF turns southward at 0400 ST. The FAC strengths show minor differences between these two sets of simulations with the most notable differences occurring at 0500 ST as seen by the inflection in the EUV CV Model trace for the March

interval. The  $\Phi_C$  traces are also quite similar with the most notable difference being the fact that the December  $\Phi_C$  is slightly higher than the June  $\Phi_C$  throughout the southward interval for the EUV CV Model runs while in the Basic CV Model runs these  $\Phi_C$  are essentially the same. This comparison provides the first clear indication that local application of the EUV limited on particle flux is having macroscopic consequences.

[21] Prior to the arrival of the southward IMF, the June interval has a higher  $\Phi_C$  as seen in Figure 2. It slowly decreases until the arrival of the southward IMF. The March and December simulations show a more nearly constant  $\Phi_C$  during this period with the March case having a slightly higher  $\Phi_C$ . Immediately after the southward IMF arrives we see a clear rise in  $\Phi_C$ , with the rate of increase being smallest for the June interval and strongest for the March interval. The March  $\Phi_C$  rises to a higher value on average and shows more variability in amplitude. As previously mentioned the December interval has a slightly higher  $\Phi_C$  than the June interval in the EUV CV Model set of simulations. Seasonal variations in the statistical average of the  $\Phi_C$  maximum, as reported by *Weimer* [1995] which are most pronounced during periods with small IMF  $B_Y$ . The statistical patterns show that the  $\Phi_C$  difference is slightly less for the sunlit hemisphere when IMF  $B_Y$  is positive which is opposite to the results we show here.

[22] *Fedder and Lyon* [1987] showed that the integrated current-voltage relationship of the MI system is similar to that of a simple circuit with a generator and its internal resistance connected an external resistor (the ionosphere), as originally proposed by *Hill* [1984]. Since the solar wind electric field is the same for each of these configurations we expect the generator voltage to be the same. So in order to explain the ordering of FAC present in Figure 2, we need to

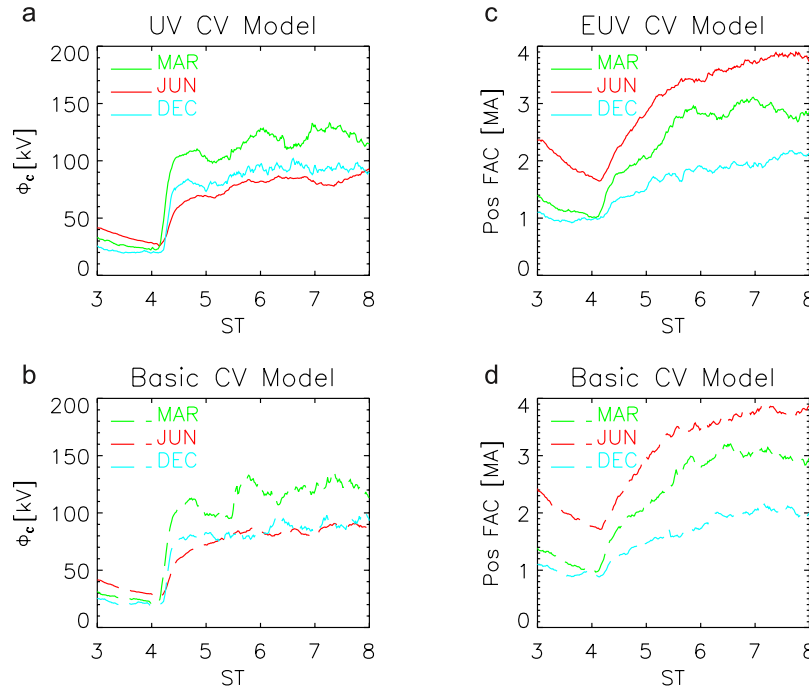


**Figure 2.** Results for a series of global Northern Hemisphere ionospheric diagnostics are displayed for each of the dipole tilt angles. (a and b) The cross polar cap potential,  $\Phi_C$ , and (c and d) the integrated field aligned current flowing out of the ionosphere. In each panel the March results are shown with the green line, the June results are shown in red, and the December results are shown in blue. In Figures 2a and 2c, results from the EUV CV Model are shown with the solid lines, and Figures 2b and 2d contain results from Basic CV Model displayed with long dashed lines.

expand upon the simple circuit analogy. Instead of considering the ionosphere as a single resistor, we generalize the model to include two resistors, one for each hemisphere, connected in parallel in place of the single resistor in the original simple circuit. In this system, the summer hemisphere will have the highest conductance and therefore the largest current should flow through this hemisphere for a constant voltage solar wind dynamo. This generalized circuit model is consistent with the ordering of March, June, and December current strengths. The ordering of the field-aligned currents is in agreement with results of interhemispheric asymmetries seen in the statistical FAC patterns deduced by, e.g., *Fujii et al.* [1981] and *Fujii and Iijima* [1987]. *Papitashvili et al.* [2002] used high-precision magnetic field data from the Oersted and MAGSAT satellites to determine a ratio of 1.57 for the Northern Hemisphere summer to Southern Hemisphere winter integrated currents and a ratio of 1.0 for the equinox case. In our results we see a value of 1.8 for the summer to winter ratio and 1.0 for the equinox case. The simple circuit analogy does not accurately capture all aspects of the MI coupling process since it predicts the same cross polar cap potential for the summer and winter hemispheres which is only seen in the Basic CV Model results. Furthermore this simple circuit analogy completely disregards any input from the magnetotail which influences the evolution of the system.

[23] Figure 3 shows the sum of the currents flowing through both hemispheres for the March and June intervals. The currents flowing through each hemisphere for the March case are the same with roughly equal contributions from each

hemisphere. A comparison of the sum of the current flowing through each hemisphere for each case reveals several interesting features. First, the total current flowing in the circuit during northward IMF is greater during the June solstice case, which is a consequence of the larger current present in the Northern (sunlit) Hemisphere. After the IMF turns southward the total current flowing through the circuit is roughly the same in June and March intervals until approximately 0515 ST when the total current in the March case increases dramatically and remains stronger than the total current in the June case. The agreement prior to 0515 ST is strong verification that our efforts to have the same driving conditions in the solar wind regardless of dipole tilt have been effective.

[24] The most significant impact of using an illumination-based limit on parallel potential drops is on the energy input into the ionosphere. Figure 4 compares the seasonal variation in the total power in electron precipitation into the Northern Hemisphere for each of the simulation sets. The characteristic energy of the precipitating electrons before they are energized by any field-aligned potential drop multiplied by the flux,  $\mathcal{E}_M F$ , and integrated over the entire hemisphere for the EUV CV Model set of simulations, is also displayed. The value of this parameter for the Basic CV Model set of runs is not shown since it is essentially the same. It is interesting to note the difference in this parameter between the March and June intervals. The March interval has a higher value for  $\mathcal{E}_M F$  with the majority of this difference arising from the  $F$ . This difference is a small fraction of the total precipitation energy and makes a small

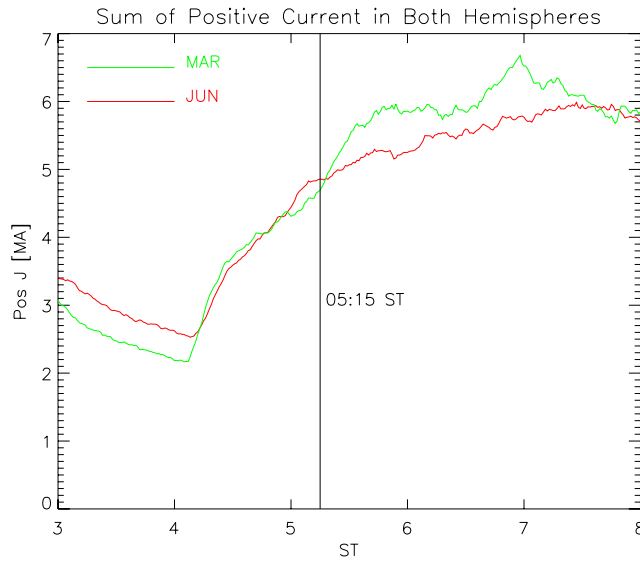


**Figure 3.** The sum of the currents flowing through each hemisphere is plotted for the March (green) and June solstice (red) simulation intervals for the EUV CV Model set of simulations. The June interval shows more total current prior to the arrival of southward IMF at 0400 ST followed by an interval of roughly the same current strength flowing into both hemispheres. A clear difference in current strength is seen at approximately 0515 ST.

contribution to the difference between the seasonal runs, especially given the large difference seen with the EUV CV Model. The difference between  $\mathcal{E}_M F$  and the total precipitation power is the contribution from the parallel potential drop. On the macroscopic scale, we see that the formulation expressed in equation (8) has the intended effect, namely a dramatic reduction in potential drop for the June interval with a modest effect during March, and a very minor effect in December. Examining the results in more detail we see that the hemispheric power for the EUV CV Model June interval is nearly the same as that for the winter interval, especially in the period prior to 0700 ST. The hemispheric power during this period in the sunlit summer hemisphere is 5–10% greater than in the dark winter hemisphere, while in

the Basic CV Model results the power flowing into the sunlit hemisphere is greater by a factor of two. Using Polar UVI images, *Liou et al.* [2001] found that more power flows into the dark hemisphere. Thus the new CV relation of equation (8) has brought the simulation results more in line with these observations. However, the trend in the simulation with more precipitation power in the sunlit hemisphere still does not agree with the UVI data, although the agreement is stronger if we discount the baseline difference in background energy flux which is primarily due to differences in the sound speed at the inner boundary related to dipole tilt effects. It is important to note that the EUV CV Model simulations also show a significant reduction in energetic electron precipitation into the afternoon sector which is in good agreement with the observations.

[25] Interestingly, the new CV relationship has had a significant impact on the evolution of the hemispheric power during the March interval. At the beginning of the period, prior to 0500 ST, the EUV CV Model trace in Figure 4 shows a reduction in the energy flux, reflecting the reduction in the energy coming from the dayside region 1 current, which is at least partially illuminated. The energy flux for the EUV CV Model results showed two clear inflections in energy input, the first at approximately 0520 ST, and the second occurring at 0625 ST. The curve for the simulation using the Basic CV Model is much smoother with a minor inflection occurring around 0515 ST and the peak being reached near 0635 ST. We interpret these inflections as sudden increases of energy associated with the formation and propagation of a plasmoid seen in the magnetotail.

[26] In Figure 5 we present the results of a calculation of the ground magnetic field perturbations for an auroral zone magnetometer located near midnight magnetic local time, using the techniques described by *Wiltberger et al.* [2003]. It is clear from this plot that the conductance changes created by the EUV CV relationship have had a significant impact on the evolution of ionospheric current systems as driven by the magnetosphere. The changes are smallest in the Northern (unlit) Hemisphere December interval results with the EUV CV Model results showing slightly more activity. In the March interval, the EUV CV Model version shows two very clear perturbations, the first one occurring at approximately 0525 ST and the second one occurring near 0635 ST.

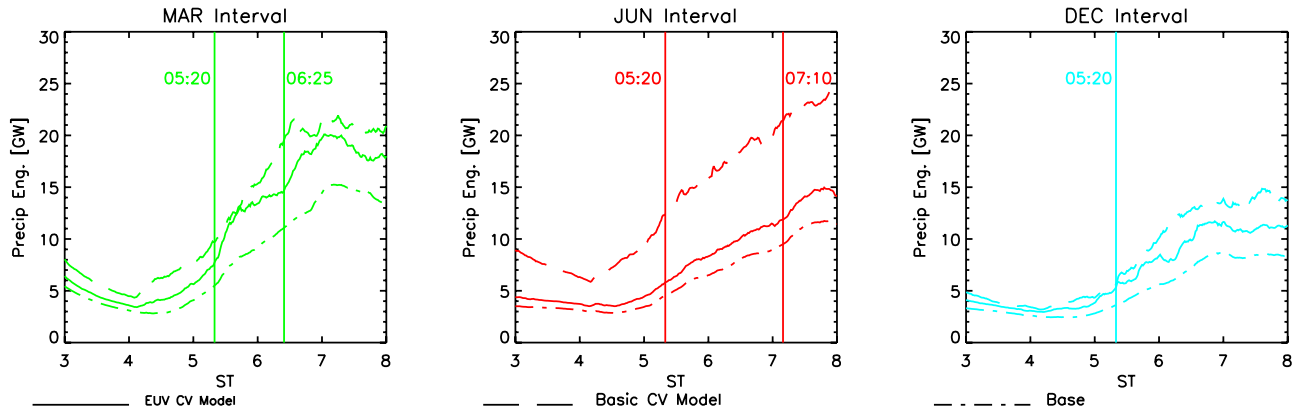


**Figure 4.** Hemispheric precipitation energy for the Northern Hemisphere is displayed for (left) the March interval, (middle) the June interval, and (right) the December interval. The results from the EUV CV Model are shown with solid lines while the results from the Basic CV Model are shown with long dashed lines. In addition, the value of  $\mathcal{E}_M F$  for the EUV CV Model is plotted with the dash-dotted line.



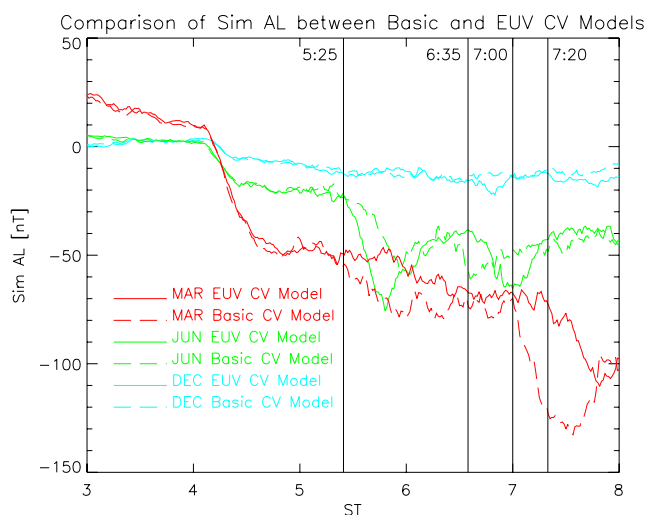


**Figure 5.** Ground magnetic field perturbations for an auroral zone magnetometer located at midnight. Keeping with the previous line and color conventions, results from the EUV CV Model set of simulations are shown with the solid lines, and the Basic CV Model set simulations are shown with the long dashed lines. The color convention is also the same with March in green, June in red, and December in cyan.

The first perturbation occurs 3 min after the inflection seen in the energy flux, while the second perturbation occurs 12 min after the second inflection in the energy flux. The Basic CV Model has a similar evolution with two perturbations with the first perturbation occurring 3 min prior to the peak seen in the EUV CV Model run. The interval between peaks is significantly shorter in the Basic CV Model results with the second peak occurring 12 min earlier. The changes in the Northern (sunlit) Hemisphere June interval results are quite intriguing. The Basic CV Model shows a small perturbation around the same time as the first perturbation in the Basic CV Model March interval and a second, much larger and more clearly defined perturbation occurring at 0700 ST. In the EUV CV Model results, the first peak is suppressed entirely and the second peak is delayed until nearly 0720 ST.

[27] The results from the hemispheric power and simulated magnetometer responses show that the ionospheric conductance can have a direct impact on the evolution of the magnetosphere and local current systems. When the parallel potential drop is limited by local EUV conductance we see that ionospheric signatures of substorm activity are more frequent and pronounced during the March interval, when the auroral zone in both hemispheres are in darkness, than during the June interval. In addition, in the simulations with Basic CV relationship, the structure of the magnetic field perturbations in the June interval more closely resembles the March interval with two perturbations present. It should also be noted that we have focused on the differences between the June and March intervals since the signatures are most pronounced in the Northern (sunlit) Hemisphere for these intervals. The Southern Hemisphere (sunlit) for the December interval has characteristics similar to the Northern Hemisphere for the June interval.

[28] Selected frames from a scientific visualization, produced by CISM-DX [Wiltberger et al., 2005b] are shown in Figure 6. The complete animation is included as auxiliary

material to this paper.<sup>1</sup> Each frame of the dynamic visualization shows the global configuration of the northern ionosphere of the EUV CV Model results for each interval. The visualization runs from 0300 ST to 0800 ST while only three times are shown in Figure 6.

[29] The beginning of Animation S1 is shown in Figures 6a, 6d, and 6g. In all three cases we see weak energy flux near 60° magnetic latitude across a broad range of MLTs centered around 0000 MLT. The energy flux appears strongest in the March interval. We describe this energy flux as the main component of the diffuse aurora since it is at low energy, has not undergone significant parallel acceleration, and is broadly distributed. All of the convection patterns show a tilt in the direction of the convection throat toward the afternoon sector, which is caused by the  $B_Y$  component of the IMF. The June plot most clearly shows the common asymmetric  $\Phi_C$  pattern with a dominant dawnside cell. The convection pattern seen here remains relatively stable during the remainder of the northward IMF portion of the interval. The diffuse auroral energy flux continues to diminish during this period. Just prior to the arrival of the southward IMF it is nearly absent in all three simulations. This as a clear indication that we have reached a very quiet magnetosphere.

[30] In Animation S1 after the arrival of southward IMF we can see the growth of the standard two cell convection pattern expected for these solar wind conditions. The effect of IMF  $B_Y$  is not nearly as pronounced during this portion of the simulations as it was under the northward conditions, especially for the June simulation. It shows only a slight difference in cell strengths and a small displacement of the peaks in local time. The December case has a slightly more pronounced asymmetry in cell strengths and a clear displacement of the peaks, with the duskside peak below the dawn-dusk line and the dawnside peak above the line. The March interval pattern is similar to the June interval, but with a much stronger convection pattern.

[31] Figures 6b, 6e, and 6h show the configuration of the ionosphere at 0530 ST, shortly after onset time determined from the simulated magnetometer response for the March interval. The energy shows a strong enhancement in both the premidnight and postmidnight portion of the auroral region at equinox. This enhancement is not seen in the June interval and was only weakly present on the premidnight side in the December case. A careful examination of the FAC structure shows that this enhancement is due to an energy increase in the precipitation caused by the parallel potential drop. The structure of this current system and its resulting distortion of the potential pattern is associated with the formation of a current wedge structure in the premidnight sector. This auroral activity is occurring in the portion of the ionosphere that is not illuminated by the Sun in the March interval. The weakness of the enhancement in the energy flux during the December interval is an indication of the influence that the conjugate hemisphere has on the evolution of the magnetosphere. As the IMF continues to remain southward we see an expansion of the auroral activity across the night side. In addition, we see enhancements of the energy flux on the dayside associated with the upward current regions.

<sup>1</sup>Auxiliary materials are available in the HTML. doi:10.1029/2008JA013108.



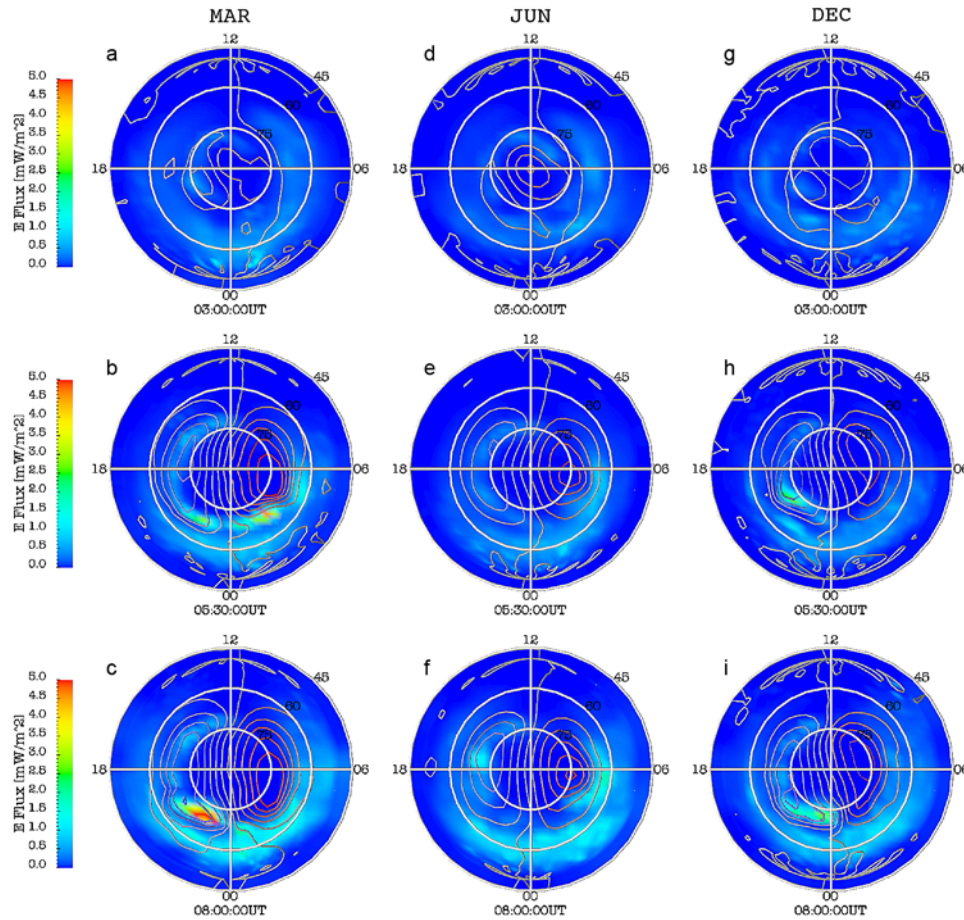


**Figure 6.** Frames taken from a scientific visualization which is part of this paper. The configuration of the simulated ionosphere in the Northern Hemisphere at selected times during each simulation for (a–c) March, (d–f) June, and (g–i) December. In each panel the contours of potential are shown on top of the energy flux. The contour intervals (10 kV) and color ranges are the same for each simulation interval. The plots are oriented with noon up and dusk on the left. In addition, the rings are spaced at 15° magnetic latitude intervals. Figures 6a, 6d, and 6g show the configuration at 0300 ST, an hour before the arrival of southward IMF. Figures 6b, 6e, and 6h show the configuration at 0530 ST, and Figures 6c, 6f, and 6i show state at the end of the simulation interval (0800 ST).

[32] Figures 6c, 6f, and 6i show the results at the end of each simulation interval. The March case has the strongest energy fluxes on the night side with significant regions of flux enhancements in the predawn sector as expected during the recovery phase of a substorm. Interestingly, the greatest energy fluxes in the June case are most pronounced on the dayside, occurring in both locations of the region 1 currents on the dusk side and where a weak region 2 current has formed on the dawnside. In addition to these enhancements there is a brightening primarily due to the diffuse component of the auroral flux on the night side. The December interval shows two main regions of enhancement of energy flux. The first is due to the region 1 current location on the dusk side below the dawn-dusk line. The second is a region of diffuse energy flux on the duskside with a small portion located just prior to midnight that is related to a weak upward current region.

#### 4. Summary

[33] In this paper we have presented results from LFM simulations for different seasons with the solar wind con-

ditions chosen so that effective driving conditions are the same. We compared the results of two classes of LFM simulations with different methods for determining the energy flux for precipitating electrons into the ionosphere. In one set a basic current-voltage relationship is used to determine the parallel potential drop effecting the precipitating electrons, namely that the drop is linear with current and inversely proportional to the source region density. In the other set we modified the current-voltage relationship by introducing a limit on how low the magnetospheric density can be based upon the local EUV driven Pedersen conductance. This technique does not directly address the physical mechanisms for the reduction in parallel potential drop; it only assures they occur in regions of high solar illumination. Using these simulations we are able to study the impact of limiting the parallel potential drop on the coupled magnetosphere-ionosphere system.

[34] The simulation results for both cases shows a clear ordering (June > March > December) of the FAC current strengths. Moreover, the ratio of Northern to Southern Hemisphere current strengths is in close agreement with

the observations. Since our implementation of the current-voltage relationship contains a linear dependence of the energy flux on the FAC current strength, the Basic CV Model results have significantly more energy flux in the June interval. Using the EUV CV relationship we are able to bring the flux into “summer” hemisphere down while not dramatically effecting the flux into the “winter” hemisphere. This brings the simulation results into closer agreement with the observations.

[35] The change in energy flux and its subsequent impact on the ionospheric conductance dramatically affects the evolution of the magnetosphere. In the EUV CV Model results auroral signatures of substorm activity are more pronounced than in the Basic CV Model results. In particular, during the June interval we observe only one onset signature in the EUV CV model results while the original formulation has two. A comparison of the energy flux into the auroral zone shows a clear flux enhancement in the March interval which is suppressed in the June simulation when the EUV CV Model is used. So the utilization of the EUV CV Model brings the energy flux properties into better agreement with the observations and results in a suppression of geomagnetic activity in the solstice conditions.

## Appendix A: Derivation of Equation (6)

[36] We assume a parallel electric field,  $E_{\parallel}$ , is sustained by an anomalous resistivity,  $\eta_{\text{eff}}$ , in regions of field-aligned current. We can integrate  $E_{\parallel} = \eta_{\text{eff}} J_{\parallel}$  across the anomalous resistive layer of field-aligned extent  $\Delta\ell = \ell_2 - \ell_1$ , where  $\ell_2$  and  $\ell_1$  are upper and lower altitude boundaries of the layer where the electric potential  $\Phi(\ell_1) = V$  and  $\Phi(\ell_2) = 0$ . We also assume the electrostatic condition,  $E_{\parallel} = -\nabla_{\parallel}\Phi$ , and  $J_{\parallel}/B = \text{constant}$  along the magnetic field. Then

$$V = \frac{J_{\parallel}}{B} \int_{\ell_1}^{\ell_2} \eta(\ell) B(\ell) d\ell. \quad (\text{A1})$$

[37] For a thin layer, the parameters characterizing the ambient plasma and magnetic field are approximately constant for  $\ell_1 \leq \ell \leq \ell_2$ . Defining

$$\bar{\eta} = \frac{1}{\Delta\ell} \int_{\ell_1}^{\ell_2} \eta(\ell) d\ell, \quad (\text{A2})$$

we then have  $V = J_{\parallel} \bar{\eta} \Delta\ell$ .

[38] A classical form for the resistivity is assumed so that  $\bar{\eta} = \bar{\nu} m_e / ne^2$  where  $n$  is the approximately constant density of current-carrying electrons in the thin resistive layer. In terms of the effective mean free path,  $\ell_{\text{MFP}}$  of the current carrying electrons,  $\bar{\nu} = v_{\text{the}} / \ell_{\text{MFP}}$  where  $v_{\text{the}}$  is the approximately constant thermal speed of current-carrying electrons in the layer. Thus,

$$\varepsilon_{\parallel} = eV = QJ_{\parallel} \quad (\text{A3})$$

where

$$Q = \frac{m_e v_{\text{the}}}{ne} \frac{\Delta\ell}{\ell_{\text{MFP}}}. \quad (\text{A4})$$

[39] If we may assume that  $n$  and  $v_{\text{the}}$  scale linearly with the MHD mass density  $\rho$  and sound speed  $c_s$  at the low-altitude boundary of the simulation, and  $\Delta\ell/\ell_{\text{MFP}} \approx \text{constant}$ , then from equation (A4) it follows that

$$\varepsilon_{\parallel} = eV = \frac{R\varepsilon_M^{1/2}}{\rho} J_{\parallel} \quad (\text{A5})$$

where  $R$  is a constant. A key assumption of this relation is  $\Delta\ell/\ell_{\text{MFP}} \approx \text{constant}$ . In the future, we will investigate alternative formulations of the anomalous resistivity that relax this assumption.

[40] Satellite measurements in downward current regions indicate that for a given amplitude of the field-aligned current the statistically observed potential drop is a fraction of that observed in upward field-aligned currents of the same amplitude [Cattell *et al.*, 2004]. Event studies show that the potential drop in downward current regions is distributed in the form of discrete double layers [Andersson *et al.*, 2002]. Theory indicates that double layer electric fields sustain smaller potential drops for a given amplitude of field-aligned current than the turbulent electric fields found in upward current regions [Lysak and Hudson, 1987]. These kinetic effects are modeled in the LFM simulation by simply choosing  $R$  to be  $5\times$  larger in upward field-aligned currents than in downward field-aligned currents.

[41] **Acknowledgments.** This material is based upon work supported by CISM which is funded by the STC Program of the National Science Foundation under agreement ATM-0120950 and by NASA grants NAG5-12652, NNG056J706, and NNX07AQ166. The National Center for Atmospheric Research is sponsored by the National Science Foundation. We would also like to thank Slava Merkin for his helpful conversations during the preparation of this paper. W.L. would like to acknowledge the sponsorship of the UCAR Faculty Fellowship Program.

[42] Zuyin Pu thanks the reviewers for their assistance in evaluating this paper.

## References

- Akasofu, S. (1981), Energy coupling between the solar wind and the magnetosphere, *Space Sci. Rev.*, 28, 121.
- Andersson, L., R. E. Ergun, D. L. Newman, J. P. McFadden, C. W. Carlson, and Y. J. Su (2002), Characteristics of parallel electric fields in the downward current region of the aurora, *Phys. Plasmas*, 9(8), 3600.
- Berthelier, A. (1990), Comment on “The universal time variation of magnetic activity,” *Geophys. Res. Lett.*, 17, 307.
- Boris, J. P. (1970), A physically motivated solution of the Alfvén problem, *Tech. Rep.*, 2167, Nav. Res. Lab., Washington, D. C.
- Cattell, C., J. Dombeck, W. Yusof, C. Carlson, and J. McFadden (2004), FAST observations of the solar illumination dependence of upflowing electron beams in the auroral zone, *J. Geophys. Res.*, 109, A02209, doi:10.1029/2003JA010075.
- Cattell, C., J. Dombeck, C. Carlson, and J. McFadden (2006), FAST observations of the solar illumination dependence of downgoing auroral electron beams: Relationship to electron energy flux, *J. Geophys. Res.*, 111, A02201, doi:10.1029/2005JA011337.
- Cliver, E. W., Y. Kamide, and A. G. Ling (2000), Mountains versus valleys: Semiannual variation of geomagnetic activity, *J. Geophys. Res.*, 105, 2413.
- Fairfield, D. H., and N. F. Ness (1967), Magnetic field measurements with the IMP 2 satellite, *J. Geophys. Res.*, 72, 2379.
- Fedder, J. A., and J. G. Lyon (1987), The solar wind-magnetosphere-ionosphere current-voltage relationship, *Geophys. Res. Lett.*, 8, 880.
- Fedder, J. A., S. P. Slinker, J. G. Lyon, and R. D. Elphinstone (1995), Global numerical simulation of the growth phase and the expansion onset for substorm observed by Viking, *J. Geophys. Res.*, 100, 19,083.
- Fridman, M., and J. Lemaire (1980), Relationship between auroral electron fluxes and field aligned electric potential difference, *J. Geophys. Res.*, 85(A2), 664.
- Fujii, R., and T. Iijima (1987), Control of the ionospheric conductivities on large-scale Birkeland current intensities under geomagnetic quiet conditions, *J. Geophys. Res.*, 92, 4505.

- Fujii, R., T. Iijima, T. A. Potemra, and M. Sugiura (1981), Seasonal dependence of large-scale Birkeland currents, *Geophys. Res. Lett.*, **8**, 1103.
- Goodrich, C. C., M. Wiltberger, R. E. Lopez, K. Papadopoulos, and J. G. Lyon (1998), An overview of the impact of the January 10–11, 1997 magnetic cloud on the magnetosphere via global MHD simulation, *Geophys. Res. Lett.*, **25**, 2537.
- Hain, K. (1987), The partial donor method, *J. Comput. Phys.*, **73**, 131.
- Hill, T. W. (1984), Magnetic coupling between the solar wind and magnetosphere: Regulated by ionospheric conductance?, *Eos Trans. AGU*, **65**, 1047.
- Horton, W., and I. Doxas (1998), A low-dimensional dynamical model for the solar wind driven geotail-ionosphere system, *J. Geophys. Res.*, **103**, 4561, doi:10.1029/97JA02417.
- Huang, C.-L., H. E. Spence, J. G. Lyon, F. R. Toffoletto, H. J. Singer, and S. Sazykin (2006), Storm-time configuration of the inner magnetosphere: Lyon-Fedder-Mobarry MHD code, Tsyganenko model, and GOES observations, *J. Geophys. Res.*, **111**, A11S16, doi:10.1029/2006JA011626.
- Hull, A. J., J. W. Bonnell, F. S. Mozer, J. D. Scudder, and C. C. Chaston (2003), Large parallel electric fields in the upward current region of the aurora: Evidence for ambipolar effects, *J. Geophys. Res.*, **108**(A6), 1265, doi:10.1029/2002JA009682.
- Johnson, M. T., J. R. Wygant, C. Cattell, F. S. Mozer, M. Temerin, and J. Scudder (2001), Observations of the seasonal dependence of the thermal plasma density in the Southern Hemisphere auroral zone and polar cap at 1RE, *J. Geophys. Res.*, **106**, 19,023, doi:10.1029/2000JA900147.
- Johnson, M. T., J. R. Wygant, C. A. Cattell, and F. S. Mozer (2003), Seasonal variations along auroral field lines: Measurements from the Polar spacecraft, *Geophys. Res. Lett.*, **30**(6), 1344, doi:10.1029/2002GL015866.
- Kan, J. R., and L. C. Lee (1979), Energy coupling function and solar wind-magnetosphere dynamo, *Geophys. Res. Lett.*, **6**, 577.
- Kelley, M. C. (1989), *The Earth's Ionosphere: Plasma Physics and Electrodynamics*, Academic, San Diego, Calif.
- Knight, S. (1973), Parallel electric fields, *Planet. Space Sci.*, **21**, 741.
- Liou, K., P. T. Newell, and C. I. Meng (2001), Seasonal effects on auroral particle acceleration and precipitation, *J. Geophys. Res.*, **106**, 2643.
- Lopez, R. E., C. C. Goodrich, M. Wiltberger, and J. G. Lyon (1998), Simulation of the March 9, 1995 substorm and initial comparison to data, in *Geospace Mass and Energy Flow: Results From the International Solar-Terrestrial Physics Program*, *Geophys. Monogr. Ser.*, vol. 104, edited by J. L. Horowitz, D. L. Gallagher, and W. K. Peterson, p. 237, AGU, Washington, D. C.
- Lyon, J. G., J. G. Fedder, and C. M. Mobarry (2004), The Lyon-Fedder-Mobarry (LFM) global MHD magnetospheric simulation code, *J. Atmos. Sol. Terr. Phys.*, **66**, 1333, doi:10.1016/j.jastp.2004.03.020.
- Lyons, L. R., D. S. Evans, and R. Lundin (1979), An observed relation between magnetic field aligned electric fields and downward electron energy fluxes in the vicinity of auroral forms, *J. Geophys. Res.*, **84**, 457.
- Lysak, R. L., and M. K. Hudson (1987), Effect of double layers on magnetosphere-ionosphere coupling, *Laser Particle Beams, Part 2*, **5**, 351.
- Mayaud, P. (1974), Comment on "Semiannual variation in geomagnetic activity" by C. T. Russell and R. L. McPherron, *J. Geophys. Res.*, **79**, 1131.
- Morooka, M., and T. Mukai (2003), Density as a controlling factor for seasonal and altitudinal variations of the auroral particle acceleration region, *J. Geophys. Res.*, **108**(A7), 1306, doi:10.1029/2002JA009786.
- Newell, P. T., C. I. Meng, and K. M. Lyons (1996), Discrete aurorae are suppressed in sunlight, *Nature*, **381**, 766.
- Newell, P. T., T. Sotirelis, J. P. Skura, Meng Ching-I., and W. Lyatsky (2002), Ultraviolet insolation drives seasonal and diurnal space weather variations, *J. Geophys. Res.*, **107**(A10), 1305, doi:10.1029/2001JA000296.
- Papitashvili, V. O., F. Christiansen, and T. Neubert (2002), A new model of field-aligned currents derived from high-precision satellite magnetic field data, *Geophys. Res. Lett.*, **29**(14), 1683, doi:10.1029/2001GL014207.
- Paschmann, G., S. Haaland, and R. Treumann (2003), *Auroral Plasma Physics*, Kluwer Acad., Dordrecht, Netherlands.
- Pokhotelov, D., W. Lotko, and A. V. Streltsov (2002), Effects of the seasonal asymmetry in ionospheric Pedersen conductance on the appearance of discrete aurora, *Geophys. Res. Lett.*, **29**(10), 1437, doi:10.1029/2001GL014010.
- Raeder, J., R. L. McPherron, L. A. Frank, S. Kokubun, G. Lu, T. Mukai, W. R. Paterson, J. B. Sigwarth, H. J. Singer, and J. A. Slavin (2001), Global simulation of the Geospace Environment Modeling substorm challenge event, *J. Geophys. Res.*, **106**, 381, doi:10.1029/2000JA000605.
- Richmond, A. D. (1992), Assimilative mapping of ionospheric electrodynamics, *Adv. Space Res.*, **12**, 59.
- Ridley, A. J., K. C. Hansen, G. Tóth, D. L. De Zeeuw, T. I. Gombosi, and K. G. Powell (2002), University of Michigan MHD results of the Geospace Global Circulation Model metrics challenge, *J. Geophys. Res.*, **107**(A10), 1290, doi:10.1029/2001JA000253.
- Robinson, R. M., R. R. Vondrak, K. Miller, T. Babbs, and D. A. Hardy (1987), On calculating ionospheric conductivities from the flux and energy of precipitating electrons, *J. Geophys. Res.*, **92**, 2565.
- Russell, C. T., and R. L. McPherron (1973), Semiannual variation of geomagnetic activity, *J. Geophys. Res.*, **78**(1), 92.
- Slinker, S. P., J. A. Fedder, B. A. Emery, K. B. Baker, D. Lummerzheim, J. G. Lyon, and F. J. Rich (1999), Comparison of global MHD simulations with AMIE simulations for the events of May 19–20, 1996, *J. Geophys. Res.*, **104**, 28,379.
- Temerin, M., and C. W. Carlson (1998), Current-voltage relationship in the downward auroral current region, *Geophys. Res. Lett.*, **25**(13), 2365.
- Weigel, R. S. (2007), Solar wind time history contribution to the day-of-year variation in geomagnetic activity, *J. Geophys. Res.*, **112**, A10207, doi:10.1029/2007JA012324.
- Weimer, D. R. (1995), Models of high-latitude electric potentials derived with a least error fit of spherical harmonic coefficients, *J. Geophys. Res.*, **100**, 19,595.
- Wiltberger, M., T. I. Pulkkinen, J. G. Lyon, and C. C. Goodrich (2000), MHD simulation of the December 10, 1996 substorm, *J. Geophys. Res.*, **106**, 27,649.
- Wiltberger, M., J. G. Lyon, and C. C. Goodrich (2003), Results from the Lyon-Fedder-Mobarry global magnetospheric model for the electrojet challenge, *J. Atmos. Sol. Terr. Phys.*, **65**, 1213.
- Wiltberger, M., R. E. Lopez, and J. G. Lyon (2005a), Results from magnetospheric Gedanken experiments using the LFM, *Adv. Space Res.*, **36**, 1797, doi:10.1016/j.asr.2004.11.043.
- Wiltberger, M., R. S. Weigel, M. Gehmeyr, and T. Guild (2005b), Analysis and visualization of space science model output and data with CISM-DX, *J. Geophys. Res.*, **110**, A09224, doi:10.1029/2004JA010956.

J. A. Fedder, Icarus Research Inc., P.O. Box 30780, Bethesda, MD 20824-0780, USA. (fedder@ppdmail.nrl.navy.mil)

W. Lotko, Thayer School of Engineering, Dartmouth College, 8000 Cummings Hall, Hanover, NH 03755, USA. (wlotko@dartmouth.edu)

R. S. Weigel, Department of Computational and Data Sciences, George Mason University, 4400 University Drive, Fairfax, VA 22030, USA. (rweigel@gmu.edu)

M. Wiltberger, High Altitude Observatory, National Center for Atmospheric Research, 3080 Center Green, Boulder, CO 80301, USA. (wiltbermj@ucar.edu)